JOURNAL OF THE ROYAL SOCIETY Interface

Chitosan-mediated crystallization and assembly of hydroxyapatite nanoparticles into hybrid nanostructured films

R Kumar, K.H Prakash, P Cheang, L Gower and K.A Khor

J. R. Soc. Interface 2008 **5**, 427-439
doi: 10.1098/rsif.2007.1141

JOURNAL OF THE ROYAL SOCIETY Interface

J. R. Soc. Interface (2008) **5**, 427–439
doi:10.1098/rsif.2007.1141
Published online 14 August 2007

Chitosan-mediated crystallization and assembly of hydroxyapatite nanoparticles into hybrid nanostructured films

R. Kumar[1], K. H. Prakash[2,*], P. Cheang[2], L. Gower[3] and K. A. Khor[4]

[1]*BioEngineering, Montana Tech of the University of Montana, Butte, MT 59701, USA*
[2]*Division of Bioengineering, and* [4]*School of Mechanical and Aerospace Engineering, Nanyang Technological University, 50 Nanyang Avenue, Singapore 639798, Republic of Singapore*
[3]*Materials Science and Engineering, University of Florida, 210A Rhines Hall, Gainesville, FL 32611, USA*

The synthesis and subsequent assembly of nearly spherical nano-hydroxyapatite (nHA) particles in the presence of trace amounts of the polysaccharide chitosan was carried out employing a wet chemical approach. Chitosan addition during synthesis not only modulated HA crystallization but also aided in the assembly of nHA particles onto itself. Solvent extraction from these suspensions formed iridescent films, of which the bottom few layers were rich in self-assembled nHA particle arrays. The cross-section of these hybrid films revealed compositional and hence structural grading of the two phases and exhibited a unique morphology in which assembled nHA particles gradually gave way to chitosan-rich top layers. Transmission electron microscope and selected area electron diffraction studies suggested that the basal plane of HA had interacted with chitosan, and scanning electron microscope studies of the hybrid films revealed multi-length scale hierarchical architecture composed of HA and chitosan. Phase identification was carried out by X-ray diffraction (XRD) and Rietveld analysis of digitized XRD data showed that the basic apatite structure was preserved, but chitosan inclusion induced subtle changes to the HA unit cell. The refinement of crystallite shape using the Popa method clearly indicated a distinct change in the growth direction of HA crystallites from [001] to [100] with increasing chitosan concentration. The paper also discusses the likelihood of chitosan phosphorylation during synthesis, which we believe to be a pathway, by which chitosan molecules chemically interact with calcium phosphate precursor compounds and orchestrate the crystallization of nHA particles. Additionally, the paper suggests several interesting biomedical applications for graded nHA–chitosan nanostructured films.

Keywords: crystallization; self-assembly; nanostructure; hydroxyapatite; hierarchical architecture; Rietveld analysis

1. INTRODUCTION

Assembly and hierarchical structuring of nanomaterials is a technologically driven area of research due to the opportunities it provides for applications ranging from molecular sieves to gene delivery. The assembly of nanostructures across several length-scales is also of paramount importance in the synthesis of organized materials with advanced functions. At present, the work carried out in this area is based on physical methods such as crystal engineering (Dabbs & Aksay 2000; Colfen & Mann 2003), external patterning (Murray *et al.* 1995; Wang 1998) and molecular cross-linking (Andres *et al.* 1996; Galow *et al.* 2000). Recently, however, there are reports that hierarchically structured materials, coupled together by chemical synthesis and self-assembly, can be produced in a single reaction mixture. In such cases, the building of embedded structures of hybrid organic–inorganic materials is not directly linked to the smallest building block of these materials but to the evolution of these structures through mutual interaction over time and space (Colfen & Mann 2003; Colfen & Yu 2005). This subject has been presented in an excellent review by Colfen & Mann (2003), where the influence of macromolecules/polymers on mesoscale self-assembly, transformation of hybrid nanostructures and possible mechanisms have been discussed in detail. Depending on the nature of the polymer and interaction between the polymer and inorganic ions/primary nuclei, crystals

*Author and address for correspondence: Nanotechnology and Biomaterials Centre, Australian Institute for Bioengineering and Nanotechnology, The University of Queensland, Brisbane, Queensland 4072, Australia (prakashkithva@yahoo.com.sg).

Received 20 June 2007
Accepted 16 July 2007

grow into various morphologies and structures. For example, flower-shaped $BaSO_4$ crystals were formed in the presence of sulphonated poly(ethylene oxide)-*block*-poly(ethylene imine), dumbbell-shaped $BaSO_4$ crystals were formed in the presence of poly(ethylene oxide)-*block*-poly(ethylene-diamine tetra acetic acid) and self-assembled nanoparticle arrays of $BaSO_4$ crystals were formed in the presence of *bis*(2-ethylhexyl)-sulphosuccinate. These clearly demonstrate the influence of different macromolecules/polymers on the crystal growth and higher order structure formation through mesoscale self-assembly. In the formation of higher order structures, *self-assembled nanoparticle arrays* can form when the binding affinity of the organic molecules is sufficiently high so that the nanocrystals are so highly stabilized that no further crystal growth can take place within the aggregates. The nanoparticles can then become ordered by organic interactions at the interfaces between the hybrid building blocks. Alternatively, *mesoscale transformations and emergent nanostructures* can drive reactions and assembly respectively, when strong binding interactions between organic molecules and inorganic nuclei severely inhibit lattice construction such that colloidal aggregates containing hybrid primary particles with metastable amorphous cores are assembled. With time, the amorphous nanoparticles crystallize within the aggregates. In the latter case, oriented crystallization, lattice distortion and shape anisotropy can be expected as the polymer can be surface adsorbed and/or impose spatial constraints for crystal growth through an epitaxial relationship between lattice spacing in certain crystal faces and distances that separate functional groups periodically arranged across the organic chain (Colfen & Mann 2003).

Growth of nano-hydroxyapatite (nHA) crystallites with various combinations of macromolecules and/or polymers have been performed by several others (Gower & Tirrell 1998; Gower & Odom 2000; Rhee & Tanaka 2000, 2001; Olszta *et al.* 2003*a*,*b*; Jiang *et al.* 2005). Olszta *et al.* (2003*a*,*b*) have shown that the synthesis of nHA in the presence of poly(aspartic acid) and poly(acrylic acid) proceeds with the formation of a fluid-like mineral precursor, which crystallizes into nHA within collagen fibrils. Jiang *et al.* (2005) and Rhee & Tanaka (2000, 2001) have shown that nHA synthesized in the presence of chondroitin sulphate takes on directional aggregation with growth patterns that resemble natural bone samples at the nanoscopic level. The morphology of nHA in these studies is reportedly needle-like, rod-like or plate-like (high aspect ratio crystals) with no observable higher order structure, perhaps due to the lack of strong binding affinity of the organic molecules. It should be noted, however, that the formation of crystalline hydroxyapatite (HA, $Ca_5(PO_4)_3OH$) from the aqueous solutions of Ca^{2+} and PO_4^{3-} ions, including in bulk synthesis, is known to proceed with the precipitation of an amorphous phase and/or a series of crystalline intermediates, and that the transformation involves structural and compositional changes (Boskey & Posner 1973; Nancollas & Tomazic 1974; Meyer & Weatherall 1982; van Kemenade & de Bruyn 1987; Lazic 1995; Prakash *et al.* 2006). Therefore, soluble reactive polymers that have high binding affinity for precursors/intermediate phases may be able to form higher order, nanostructured hydroxyapatite hybrids. We used the polysaccharide chitosan as a trace organic additive (50 mg per gram of HA max.) in the synthesis media and carried out preliminary structural and morphological characterization of nHA–chitosan hybrid particles in the suspension. The films cast from the suspensions by solvent evaporation were also similarly characterized.

Chitosan is the deacetylated product of chitin, which is an abundantly present macromolecule in crustacean exoskeleton (shrimp, crab, etc.). The monomer unit in chitin and chitosan is acetyl-glucosamine (*N*-acetyl-2-amino-2-deoxy-D-gluco-pyranose) and glucosamine (2-amino-2-deoxy-D-gluco-pyranose), respectively. In both chitin and chitosan, the monomer units are linked through β-D-(1-4)-glycosidic bonds. Owing to the abundance of free amine groups on chitosan, it is both reactive (Yi *et al.* 2005; importantly it undergoes phosphorylation, Wan *et al.* 2003) and soluble as a function of pH. As such, chitosan–nHA composites have been identified as potential candidate materials for various biomedical applications including scaffolds for mineralized tissue repair. The reports on existing composites describe higher weight fractions of chitosan (up to 1.5 g per gram of HA), prepared either by physically blending nHA with chitosan solution or co-precipitating both phases chemically, followed by fabricating the mixtures into components (Varma *et al.* 1999; Yamaguchi *et al.* 2000, 2001). Rusu *et al.* (2005) have looked at the effect of size modulation and packing density of nHA crystallites embedded within a co-precipitated chitosan matrix (composition 1 g per gram of nHA). Herein, we show that chitosan, added at considerably lower concentrations (20–70 mg l^{-1} or approx. 3 wt% max.), has the ability to effectively modulate HA crystallization and simultaneously aid in the assembly of a graded and hybrid nanostructured film.

2. MATERIAL AND METHODS

2.1. Synthesis of nano-hydroxyapatite (control)

Nano-hydroxyapatite was synthesized using orthophosphoric acid, H_3PO_4, and calcium hydroxide, $Ca(OH)_2$ (both analytical grades from Sigma-Aldrich, USA). De-ionized (DI) water (Milli-Q unit, Millipore, USA) was used to prepare all the solutions/suspensions in the present study. To a 200 ml suspension containing 0.01 mol calcined $Ca(OH)_2$ (700°C for 2 hours), heated to 98°C (±2°C) under constant stirring at 600*g*, 200 ml of 0.03 M H_3PO_4 aqueous solution was added at a rate of 4 ml min^{-1} using a peristaltic pump. During the acid addition, the pH of the solution, which was constant around 11.0 over a considerable length of time, was monitored and it started to decrease rapidly towards the end of acid addition and reached close to 7.6 at the completion of acid addition. The reaction mixture was stirred for another 2 hours and then cooled to room temperature.

2.2. Synthesis of hybrid suspensions and films

Synthesis of nHA in the presence of chitosan (approx. 100 kDa, 85% deacetylated, from Sigma-Aldrich, USA) was carried out by separately adding 50 ml of chitosan solution at a rate of 2 ml min^{-1} to the reaction mixture described above, when the pH started to decrease from 11.0. Chitosan solutions were prepared by dissolving appropriate quantities of chitosan in 1 wt% acetic acid. (Acetic acid solution was prepared by diluting reagent grade glacial acetic from Sigma-Aldrich, USA.) Table 1 details the suspension code given and the chitosan concentration in the final nHA suspension. Evaporation loss of the solution was minimized by using a tight aluminium foil cover with minimal openings for the acid addition, chitosan solution and the temperature/pH probe. At the end of the additions, the pH was approximately 6 for all hybrid suspensions. The suspension was then stirred for 2 hours and cooled to room temperature. Hybrid films were formed by spreading 5 ml of the suspension onto a glass Petri dish and evaporating the solvent at 37°C in a controlled oven environment. A schematic of the process leading to the formation of the films is shown in figure 1.

2.3. Structural characterization

A Shimadzu Lab 6000X X-ray diffractometer employing CuK_α filtered radiation and a graphite secondary monochromator was used for X-ray diffraction (XRD) studies of the particles in the suspension (centrifuged and dried) and in the films (dried and crushed). The XRD scan rate was fixed at 1° min^{-1} and the step size was 0.02°. The accelerating voltage and current used were 40 kV and 20 mA, respectively. The morphology of the crystallites was observed in a JEOL 2010 transmission electron microscope (TEM) at 200 kV by dipping a copper grid into 50 times diluted suspensions. Selected area electron diffraction (SEAD) of the particles was carried out on films formed by drying a drop of diluted hybrid suspension on a copper grid. The micro-/nanostructural features of the hybrid films were examined using a JEOL 5410 scanning electron microscope (SEM) and the film cross-section using a JSM 6340 field emission SEM (FESEM). Fourier transform infrared (FTIR) spectroscopic studies (Perkin–Elmer System 2000, USA) were carried out to investigate the compositional characteristics of the hybrid-nHA particles. Samples were prepared by embedding a fixed weight of centrifuged particles in KBr and pressing the mixture into discs. An average of 40 scans at 4 cm^{-1} resolution was taken for each sample.

2.4. Rietveld refinement of XRD results

Preliminary quantitative analysis of the XRD data was carried out by Rietveld full profile fitting using Rietquan (v. 2.3) crystallographic refinement software, the details of which are reported elsewhere (McCusker *et al.* 1999; Kumar *et al.* 2004, 2005). The HA crystal model was built using the information from the International Crystal Structure Database (ICSD) for HA. The details of the HA crystallographic model are listed in table 2. Peak shapes were modelled using the pseudo-Voigt function and two asymmetry parameters were refined. In each case, four background parameters, a scale factor, five peak shape parameters, 2θ offset (zero point correction), sample displacement, cell parameters and atomic positions were refined. After refinement of the parameters, the atomic positions occupancy and

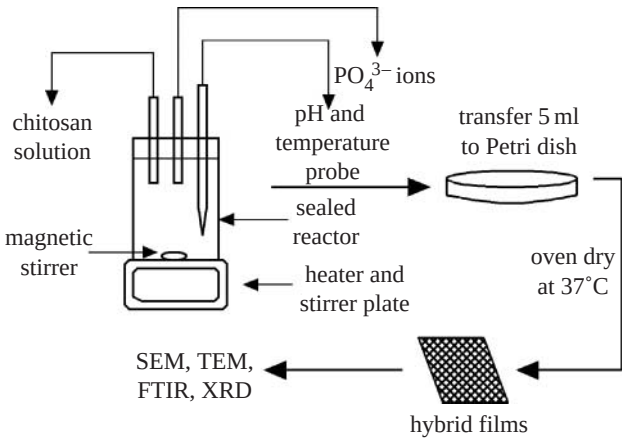

Figure 1. Schematic of synthesis and characterization experiments carried out.

Table 1. Suspension codes and the quantities of reagents used in the present study.

	reagents quantity			concentrations of chitosan[c] ($mg\,l^{-1}$)
code	$Ca(OH)_2$[a] (mmol)	H_3PO_4[a] (mmol)	chitosan[b] (mg)	
HS00	10	6	0	0
HS20	10	6	9.1	20
HS40	10	6	18.2	40
HS70	10	6	31.4	70

[a] Quantities are in 200 ml DI water.
[b] Quantity of chitosan in 50 ml of 1 wt% acetic acid.
[c] Approximate concentration of chitosan in the suspension.

Table 2. Summary of crystal parameters used for Rietveld refinement.

			lattice parameters (nm)	
phase	crystal system	space group	*a*	*c*
HA	hexagonal	$P6_3/m$	0.9422	0.6885
atomic coordinates				
atom/ion	*x*	*y*	*z*	
Ca1	0.333	0.667	0.001	
Ca2	0.246	0.993	0.250	
P	0.400	0.369	0.250	
O1	0.329	0.484	0.250	
O2	0.589	0.466	0.250	
O3	0.348	0.259	0.073	
OH^-	0.000	0.000	0.180	

thermal vibration factor for the various atomic species were refined till convergence was reached. The occupancy of the oxygen and hydrogen atoms associated with the –OH group was refined as a group (i.e. OH^- occupancy) using the same reasoning given by Knowles *et al.* (1996). Lastly, the XRD data were also refined to construct the crystallite shape and size based on the Popa model (Popa 1998) using the Rietveld method on the MAUD crystallographic computation program (v. 2.04). The software refines crystallite size using the broadening of all diffraction peaks and calculates the individual coherent lengths for the *hkl* planes under consideration and hence overall size and shapes of the crystallites. The shapes are plotted using a solid free-form method embedded in the software.

3. RESULTS

3.1. Physical appearance of hybrid suspensions

Immediately after synthesis, a distinct difference was apparent between the control and the nHA/chitosan hybrid suspensions. The hybrid suspension appeared well dispersed immediately after synthesis or after several minutes of mild sonication. The control suspension settled within 30 min while the hybrid suspensions settled after much longer time (a few weeks). The increased settling time of the hybrid suspensions could be due to the increased viscosity of the medium and smaller particle sizes. Apart from these, however, as it would be shown later, the interaction between the chitosan molecules and nHA particles has been found to play a likely role in the increased settling time of the hybrid suspensions.

3.2. Crystal structure characterization of nHA in suspension

X-ray diffractograms of the nanoparticles centrifuged from the control and hybrid suspensions are shown in figure 2 and the major peaks, as referenced from JCPDS file no. 09-432, corresponded to HA. As observed in figure 2, there is a shift in the position of the (002) and (300) peaks to lower 2θ values with increasing chitosan concentration. As a result, an increase in the *d*-spacing of these two orthogonal planes (and hence unit-cell lattice parameters) is expected. Rietveld refinement of the X-ray diffractograms revealed that the overall apatite structure was preserved. However, in confirmation of the earlier observation, there was an increasing trend in the lattice parameters of nHA crystallites with increasing chitosan concentration (table 3). It is worth mentioning that there was a new peak at around 24° next to the plane (111) at 23° and the intensity of the plane (132) at 48° was unusually high in the HS40 samples (figure 2*c*) compared with other samples, while all other peaks represent HA. After centrifugation, the drying process before performing XRD could sometimes have resulted in the extraneous crystallization of other more soluble calcium phosphates resulting in these extra and/or unusual peaks. We note that these uncharacteristic

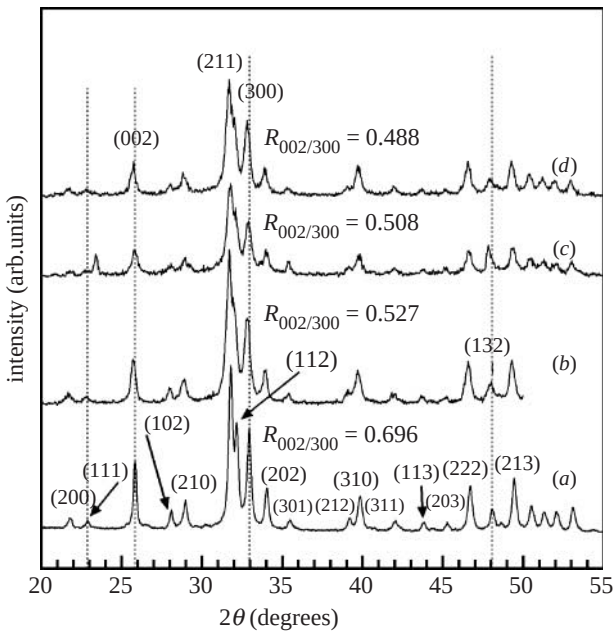

Figure 2. X-ray diffractograms of (*a*) control HA nanoparticles—HS00, (*b*) HS20, (*c*) HS40 and (*d*) HS70 HA–chitosan hybrid particles. The dashed vertical lines highlight the shifting of the (002) and (300) planes to smaller 2θ (larger *d*-spacing). The decreasing ratio $R_{002/300} = I_{(002)}/I_{(300)}$ indicates a gradual change in the orientation of crystallites, with respect to a reference plane, as the chitosan concentration is increased.

Table 3. Change in lattice parameters (nm) for HA in the presence of chitosan. (The error in the last decimal place is shown in parenthesis.)

	lattice parameter (nm)	
sample	*a*	*c*
HS00	0.9427(3)	0.6902(5)
HS20	0.9434(4)	0.6913(6)
HS40	0.9439(6)	0.6915(6)
HS70	0.9444(5)	0.6919(4)

peaks affect the accuracy of the Rietveld refinement to some extent; however, this effect is minimal considering the smooth trends in lattice parameter changes with the concentration of chitosan.

In addition, the (002) reflection was weaker and broader in the hybrid nanoparticles and the ratio of peak intensity of the planes (002) and (300), $R_{002/300} = I_{(002)}/I_{(300)}$, for the hybrid nanoparticles was smaller (figure 2*b–d*) than the control (figure 2*a*). The decreasing $R_{002/300}$ with chitosan addition and broader peaks suggested that the growth along the c-axis was suppressed and that the shape and size of these particles were modified as a function of chitosan addition. The refined shapes of the nHA particles carried out using the Popa model (Popa 1998), is shown in figure 3. The shape is described in terms of aspect ratio, that is the ratio of length in the [001] direction (height) to length in the [100] direction (diameter). The results revealed a decreasing trend in the aspect ratio of the crystallites, indicating that growth in the [001] direction was suppressed with increasing chitosan concentration.

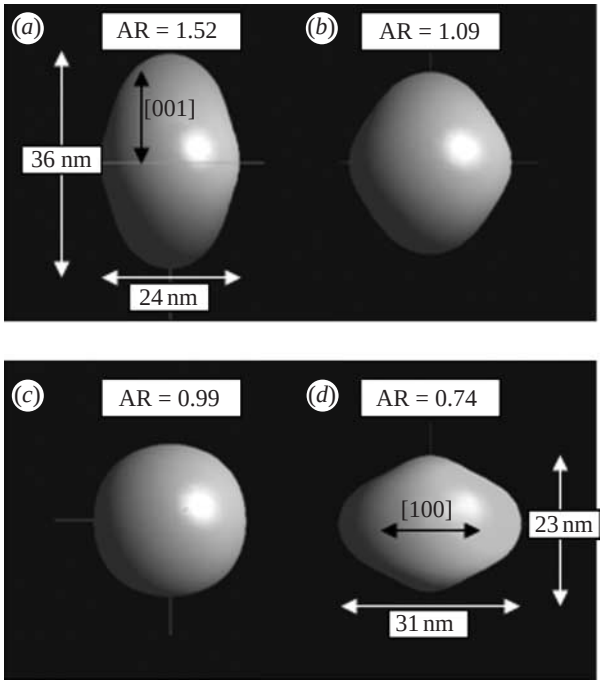

Figure 3. Crystallographically refined crystallite shapes for (*a*) HS00 (control, 0 mg l^{-1}), (*b*) HS20 (20 mg l^{-1}), (*c*) HS40 (40 mg l^{-1}) and (*d*) HS70 HA–chitosan hybrid nanoparticles (70 mg l^{-1}).

From the XRD and refinement results, it can be said that chitosan molecules interfered with the growth of nHA crystallites, though the exact nature of the interaction is not yet apparent.

3.3. Microstructural characterizations of hybrid suspensions

Representative TEM images of nHA particles in control and hybrid suspensions are shown in figure 4. The size of nHA in hybrid suspensions is visibly smaller than the control. Qualitatively speaking, the refined particle shapes and sizes shown in figure 3 correlate reasonably well with the respective particle shapes observed in TEM (figure 4). The particle size distribution also seems narrow and uniform in all samples. There was also an indication that the hybrid particles exhibited spiralled or staggered-linear arrangement (highlighted by arrows in figure 4*a* showing a coiled chain-like arrangement of nanoparticles). These studies also revealed that there were some spiraled fragments (marked by a circle in figure 4*a*) that appeared lighter owing to lower electron scattering contrast. Chitosan molecular chains in solution exist in a string-like conformation appearing as worm-like (spiral) single chains, as shown in a recent study by Pedroni *et al.* (2003). Furthermore, they have ascertained that the chain length increases with the degree of deacetylation (DDA) of chitosan or the extent of protonation of the $-NH_2$ group. Thus, the lighter spiraled features appearing in figure 4*a* could indeed be chitosan polymer chains. It is then probable, given the coiled assembly of nHA in figure 4*a*,*b*, that the HA nanoparticles were attached onto self-assembled chitosan molecular chains. The narrow particle size distribution in the hybrid suspension (figure 4*a*,*c*) also suggested that nHA growth was not non-specific but controlled by the spatial distribution of chitosan molecules.

Figure 5 shows a representative TEM image of films formed from hybrid suspensions on a copper grid and its respective SEAD pattern. The SEAD pattern (figure 5*b*) shows a ring that corresponded closely to the overlapping *d*-spacing of (211), (112) and (300) planes. There were, however, only spots for (002) and (004) planes and not rings confirming the likelihood that the nanoparticles preferentially assembled on their basal planes but were randomly rotated with respect to this plane (or did not exhibit in-plane order). The lack of in-plane order here (figure 5*a*), as opposed to SEM studies (shown next), is rationalized due to the short drying duration and dilution of the hybrid suspension employed, as we were initially interested in looking at the particles instead of the ordering phenomenon. The SEAD pattern also supports the flatter crystallite shape, obtained through Rietveld refinement of XRD results.

3.4. Microstructural characterization of hybrid films

Upon drying 5 ml of the suspension in a glass Petri dish at a relatively slower rate (37°C in an oven overnight) compared with that on TEM copper grids, translucent bluish films were obtained. The films were then lifted off the dish by stamping the top surface with adhesive carbon tape and rapidly removing the tape to observe the bottommost layers of the film closest to the dish surface. Figure 6 shows SEM images of these films, which revealed an ordered two-dimensional array of nHA particles at the bottom of the film as opposed to the control (figure 6*a*), which was randomly aggregated. The ordering (or controlled aggregation) was clearly evident in the HS20 sample where the concentration of chitosan was as low as 20 mg l^{-1}. The ordering persisted as the chitosan concentration was increased up to 70 mg l^{-1}. These results were confirmed by observations at 6–8 locations within several films, and experiments were done in triplicate to observe any variations. However, it turned out that assembly of nHA indeed occurred in all attempts. At first glance, the images in figure 6*b*–*d* look blurry, but these films have been repeatedly examined by SEM and it is confirmed that this is not owing to poor image quality but, perhaps, a real structural effect caused by this staggered-linear arrangement of HA–chitosan hybrid particles (figure 6*e*). Also the ordering was examined at this magnification (20 000×), even though actual particulate sizes were much smaller, to provide an estimation of the length-scale to which this ordering phenomenon persisted. As seen from the micrographs (figure 6*b*–*d*), the ordering was clearly over several tens of micrometers. In order to specifically implicate the importance of chitosan presence, during synthesis leading to the assembly of nHA, control nHA particles were mixed and mildly sonicated with chitosan such that the concentration of chitosan in the mixture was close to 70 mg l^{-1}. Visually, the films formed from this mixture were irregular (not translucent) and highly cracked and SEM investigation

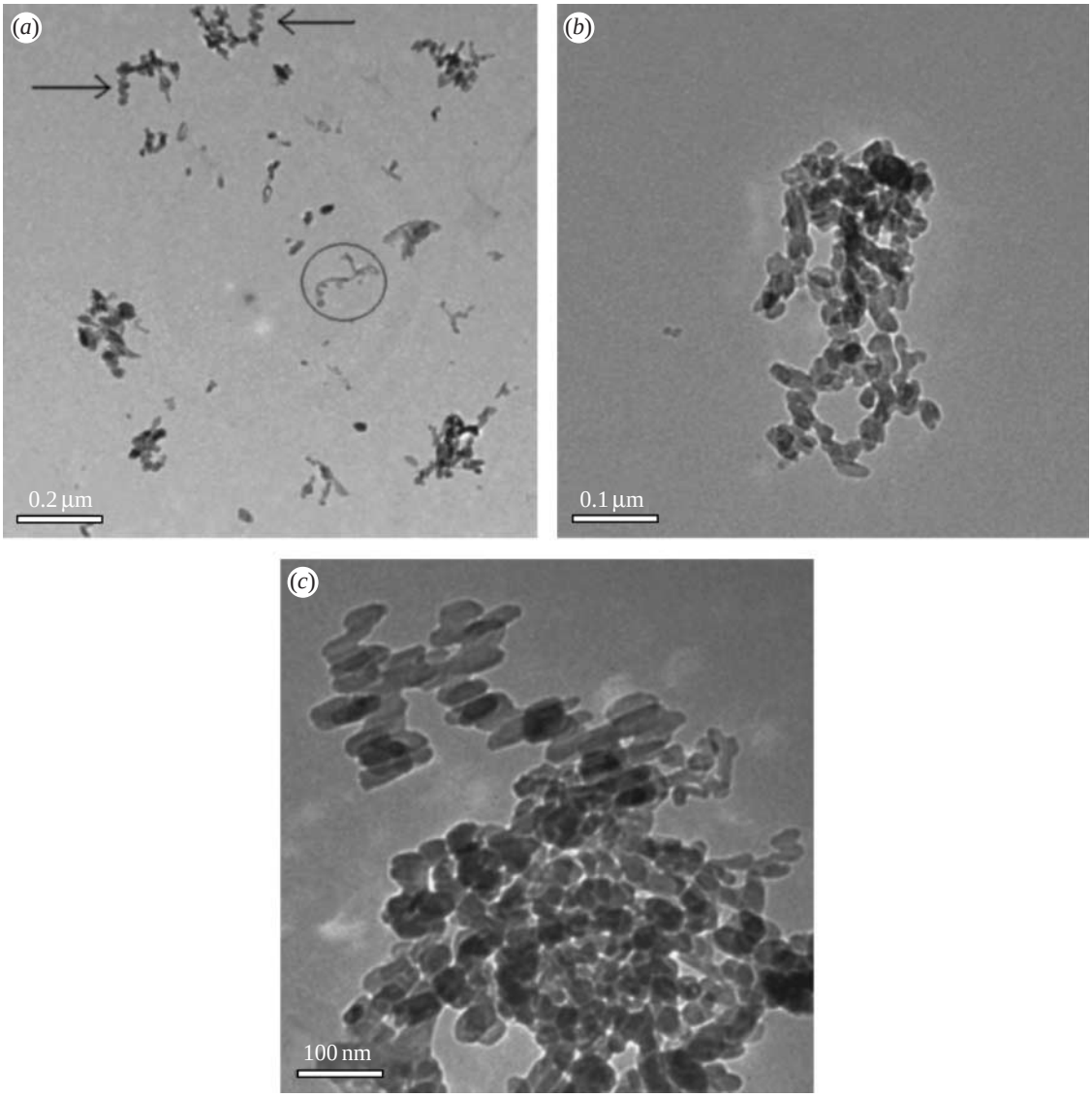

Figure 4. Nano-HA synthesized at 98°C. (*a*,*b*) HS70 and (*c*) control particles (HS00).

revealed no assembly traits (figure 6*f*). Thus it was confirmed that the presence of chitosan in the suspension, only during the synthesis of nHA, led to the observed assembly (figures 5 and 6). Quantitative phase analysis, via the Rietveld method, of films showed that there was some amount of dicalcium phosphate dihydrate, $CaHPO_4{\cdot}2H_2O$, present in the hybrid films (not shown here), while it was not present in the control nor in the centrifuged hybrid nanoparticles (figure 2). This indicated that brushite had formed only during drying and perhaps the decreasing pH and presence of unassociated Ca^{2+} and PO_4^{3-} ions might have favoured its formation (Elliot 1994).

Figure 7 shows a representative image of the cross-section of these hybrid films that exhibited another interesting structure, which started with HA nanoparticles assembled at the bottom and a continuously changing structure that ended on top with a chitosan surface. In other words, the films were incrementally graded with different amounts of chitosan and/or HA from the film/Petri dish interface (predominantly HA) to the film surface (predominantly chitosan). This implied that a film that has both the organic and inorganic components can be intimately incorporated and graded both structurally and compositionally through a gravity-assisted assembly process.

3.5. Compositional characterizations of hybrid particles

FTIR spectra of dried HA, chitosan–HA and pure chitosan films are shown in figure 8. The FTIR spectra of pure HA and chitosan were compared with that for the hybrid particles centrifuged from suspension and washed with distilled H_2O. Several bands pertinent to HA for OH^- stretch at about 3600 and the v_3 and v_4 band of the PO_4^{3-} group at 1190–970 and 660–520 cm^{-1}, respectively, were observed. Typical v_3 CO_3^{2-} bands (at 1650 cm^{-1}) indicating B-type CO_3^{2-} substitution for the PO_4^{3-} site were also noted. The FTIR spectrums of HA (Penel *et al.* 1997; Rehman & Bonfield 1997) and chitosan (Brugnerotto *et al.* 2001; Falini *et al.* 2003) are well documented, but some uncertainties regarding the resolution of data, especially for chitosan, still exist. In general, however, the spectral deformation bands for chitosan are 3450 cm^{-1} for the OH^- groups,

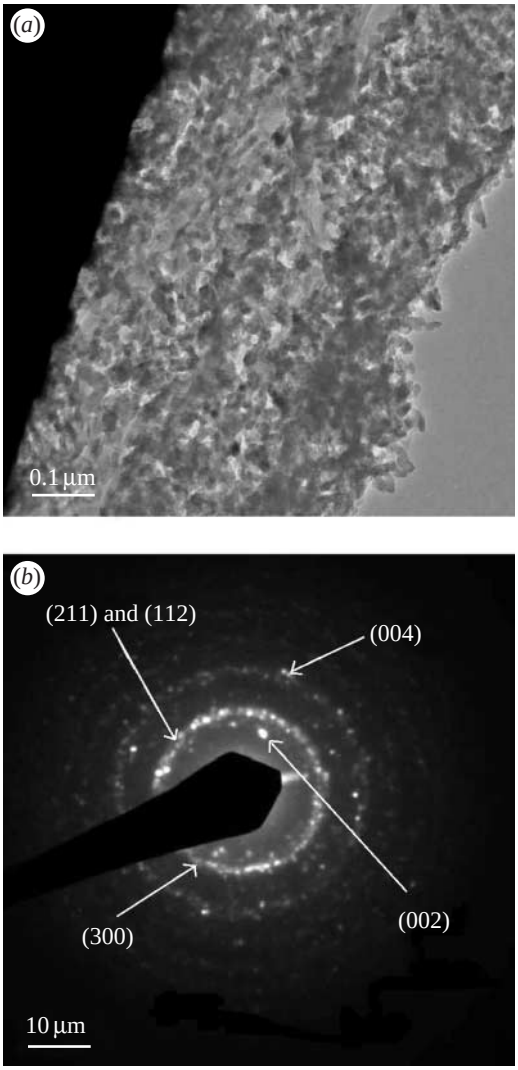

Figure 5. TEM showing (*a*) particles assembled onto Cu-grid and (*b*) SEAD of the assembled layer from the HS70 hybrid suspension.

2900 cm^{-1} for the $–CH_2$ backbone, approximately 1650–1660 cm^{-1} for the amide I (C=O) bands, approximately 1580–1590 cm^{-1} for the amine ($–NH_2$), approximately 1543–1553 cm^{-1} for the amide II (–NH) and approximately 1310 cm^{-1} for the amide III. There is a convoluted spectral peak at about 1610–1620 cm^{-1} assigned to the $–NH_3^+$ group, which is encountered for dissolved chitosan. Other than these, there are also important bands pertinent to the glucosamine unit from 1020 to 1220 cm^{-1}. However, in the hybrids they overlap with the PO_4^{3-} v_3 bands from HA and are difficult to examine without careful deconvolution.

As such most of the data from FTIR that are useful in determining interactions and functional species are between 3600 and 1200 cm^{-1}. At approximately 2900 cm^{-1}, the –CH stretch band appeared as a weak broad peak for the nHA hybrid particles (indicated with a dotted line). With increasing chitosan concentration during synthesis, notably the NH_3^+ band, at approximately 1616 cm^{-1}, appeared as a shoulder and next to the overlapping H_2O band (1629 cm^{-1}) and amide-I bands (1648 cm^{-1}). These latter bands can be considered overlapping over several wave numbers as the combined peak blue shifts by approximately 8 to 1631 cm^{-1}. Also the amide-II band (amino group) was no longer discernable. As such it can be inferred that the nHA hybrid particles contained surface-bound chitosan molecules, with protonated amine groups. The presence of only NH_3^+ bands also implied that the 'hot alkali' treatment during HA synthesis could have further deacetylated the original chitosan. Overall, the molecular structure of chitosan seemed to be subtly altered after synthesis. The addition of chitosan also affected the localized bonding structure of the PO_4^{3-} groups in HA as seen from the broadening of v_3 and v_4 PO_4^{3-}bands.

4. DISCUSSION

The experimental results from XRD, TEM, SEM and FTIR studies showed that chitosan, only when added during nHA synthesis, strongly interacted and regulated the growth of crystalline nHA and subsequently led to the formation of hybrid films composed of self-assembled nHA and chitosan. As mentioned earlier, higher order structures can be formed by the interaction of macromolecules with either crystalline nanoparticles or with the amorphous precursor compounds, of which the amorphous phase crystallizes with time within the confined field imposed by the macromolecules, leading to shape anisotropy and hybrid nanostructures (Colfen & Mann 2003; Colfen & Yu 2005). It has been shown that the formation of nHA in reaction systems similar to the present study (but without chitosan) proceeds with the formation of amorphous calcium phosphate (ACP; $Ca_3(PO_4)_2 \cdot xH_2O$) and that the transformation of ACP directly into crystalline HA starts a few minutes earlier than the pH of the reaction mixture starts to decrease rapidly (Prakash *et al.* 2006). In other words, when the pH of the reaction mixture starts to decrease rapidly, the reaction mixture contains ACP, HA crystallites and Ca^{2+} and PO_4^{3-} ions. As we have introduced the chitosan solution to the reaction mixture only when the pH started to decrease along with the H_3PO_4 solution, the chitosan molecules are likely to interact with ACP, HA crystallites and Ca^{2+} and PO_4^{3-} ions. As such, from the present experimental results, it is rather difficult to identify the exact nature of interactions that led to the assembly of hybrid nanoparticles in the films. However, the interaction between the chitosan molecules and ACP through phosphorylation of chitosan seems to be a likely mechanism. This hypothesis is supported partly by the experimental results and partly by the reported results on the physiochemical properties of chitosan.

It has been reported that chitosan interacts with inorganic ions owing to its hydrophilic and reactive nature in aqueous electrolyte solutions (Varma *et al.* 2004). Chitosan and its derivates are known for their chelation properties towards transition metal ions. However, its ability to chelate Ca^{2+} ions is poor but improves upon phosphorylation (Nishi *et al.* 1986). Moreover, in a review by Sigel & Martin (1982) it is strongly emphasized that chelation of metal ions by amine and amide groups is effective only in highly basic solutions (pH > 12) where deprotonation of $–NH_2$ groups takes place, which then bind the metal ions. In our case, however, considering the steadily decreasing

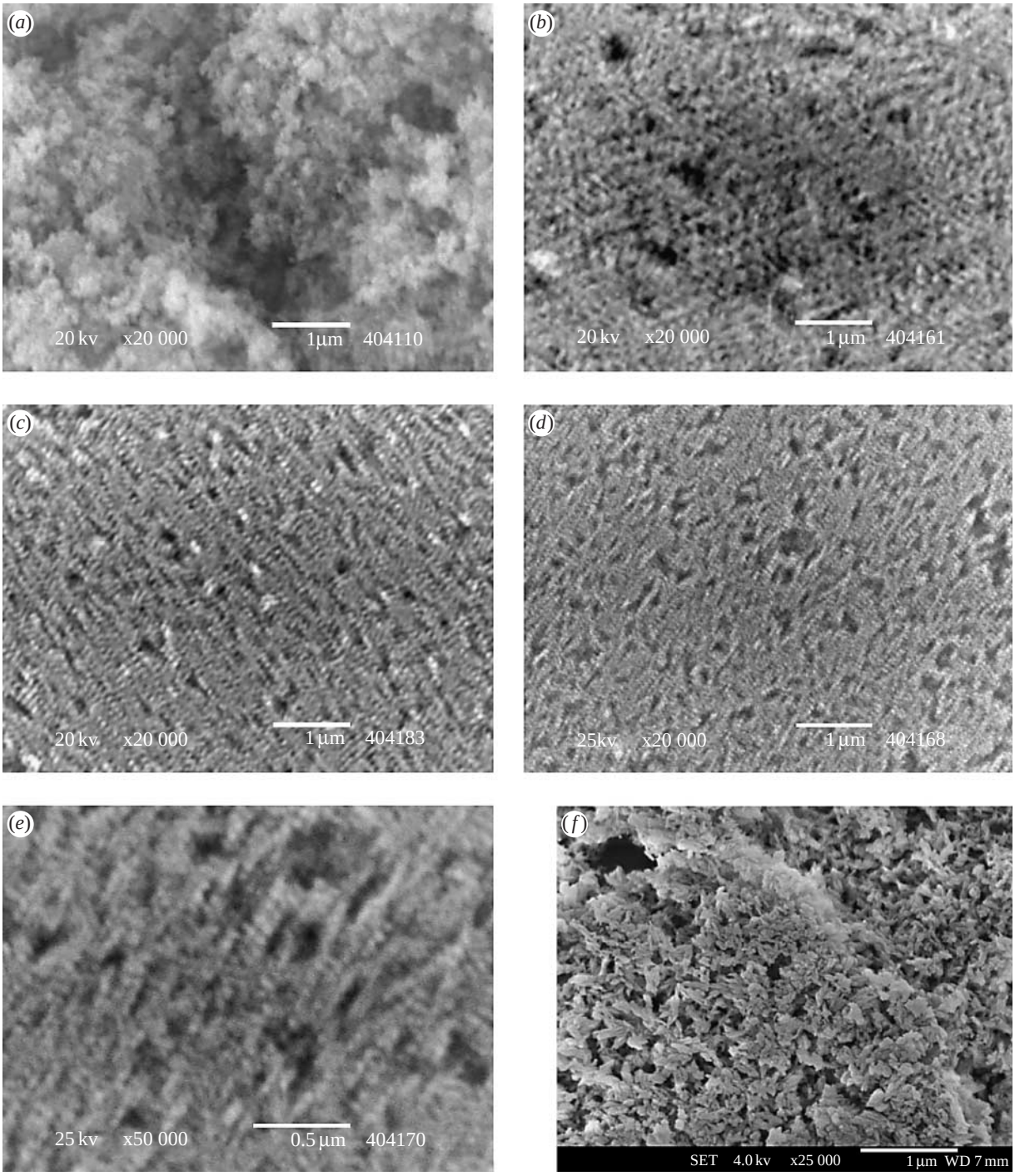

Figure 6. Self-assembly of nHA in the hybrid films from the suspensions (*a*) HS00, (*b*) HS20, (*c*) HS40, (*d*) HS70, (*e*) higher magnification of film (*d*), and (*f*) films formed by physical blending of chitosan solution and control HA particles with chitosan concentration close to HS70 samples. Scale bars, (*a–d,f*) 1 µm and (*e*) 0.5 µm.

pH of the solution and poor stability of the Ca–chitosan complex, chelation of Ca^{2+} ions by $–NH_2$ groups seems highly unlikely. A detailed study of the literature on the interaction of chitosan with PO_4^{3-} ions indicated that chitsoan has the greater affinity to react with PO_4^{3-} ions in both acidic and basic solutions and a propensity to undergo phosphorylation under the experimental conditions used in the present study. In studies specifically aimed at phosphorylating chitosan, the reagents used for phosphorylation include P_2O_5 in methanesulphonic acid (Nishi *et al.* 1986), H_3PO_3 or diethyl hydrogen phosphite in formaldehyde (Matevosyan *et al.* 2003) and urea and H_3PO_4 in dimethylformamide (Yokogawa *et al.* 2001; Wan *et al.* 2003). In these methods, PO_4^{3-}, HPO_4^{2-} or $H_2PO_4^{-}$ ions are found to react with $–NH_2$ and/or –OH groups on the chitosan molecule as represented below (Wan *et al.* 2003).

$$\begin{aligned} &–CH_2OH + PO_4^{3-} \rightarrow –CH_2–O–PO_3^{3-} \quad \text{or} \\ &–NH_2 + PO_4^{3-} \rightarrow –NH–O–PO_3^{3-} \quad \text{and} \end{aligned} \tag{4.1}$$

$$–NH_3^{+} + PO_4^{3-} \rightarrow –NH_3^{+}PO_4^{3-}. \tag{4.2}$$

Since we added chitosan solution to the reaction mixture along with the aqueous H_3PO_4 solution at the time when the pH of the reaction mixture started to decrease from approximately 11.0 and reached

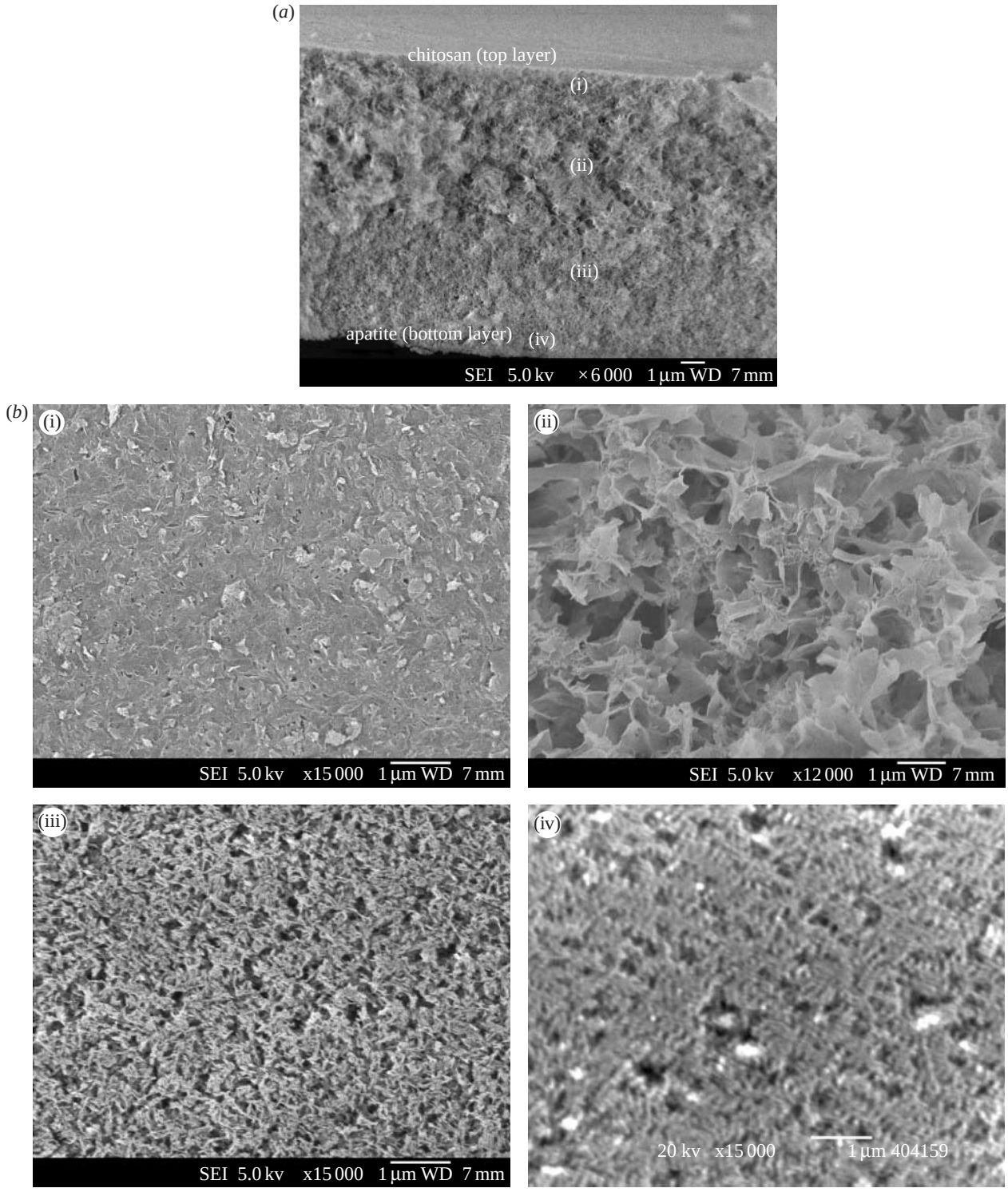

Figure 7. (*a*) Cross-section of HS70 hybrid nanostructured film showing (*b*) several levels of architecture—(i) mainly chitosan on the top of the film and (ii) the subsurface, (iii) chitosan–HA interwoven structure and (iv) assembled nHA at the bottom. Scale bar, 1 µm.

approximately 6.0 at the end of the reaction, phosphorylation of chitosan (most probably via schemes (4.1) and (4.2)) was possible. With the phosphorylated groups, chitosan can strongly bind with ACP and impose constraints on ACP to crystalline HA transformation. Owing to this, perhaps, oriented nHA crystallites formed and assembled into higher order structures. The changes in lattice parameters and the shape of the crystallites obtained through crystallographic computing (table 3 and figure 3) also support this hypothesis and implicate the likelihood of this mechanism. In contrast, if the interaction of chitosan and/or phosphorylated chitosan with primary nuclei was likely, then the change in lattice parameters and the shape of the nHA crystallites would not have been expected. Similarly, the physical blending of chitosan and nHA would be expected to yield assembled nanostructured arrays, as observed in figure 6*d*,*e*. Rather, this led to random aggregates of nHA crystallites, as shown in figure 6*f*. Therefore, it can be said, based on our present

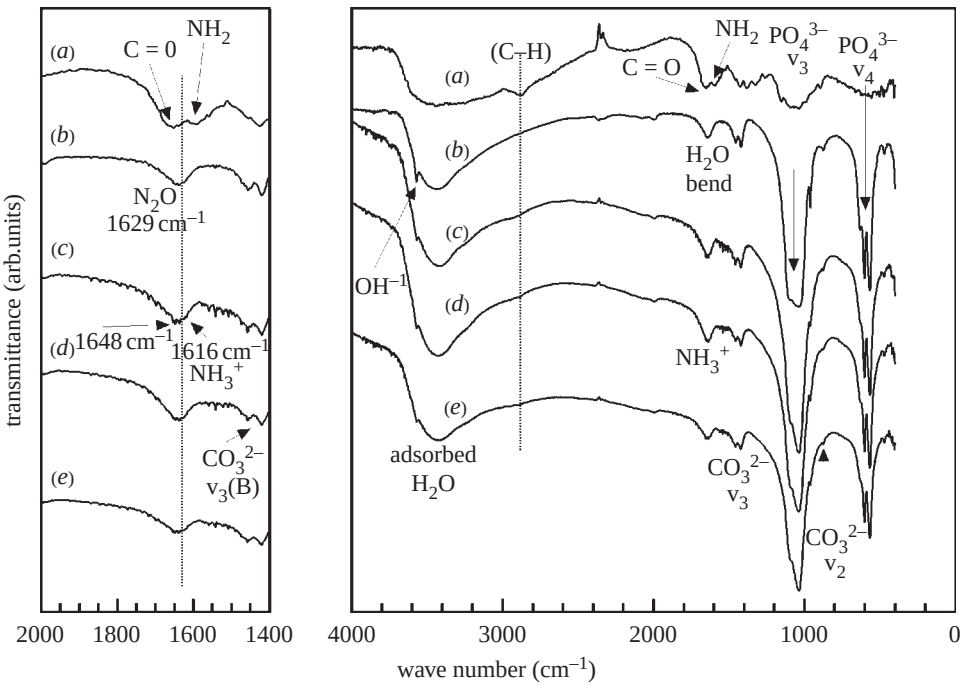

Figure 8. FTIR of (*a*) chitosan, (*b*) control nHA, (*c*) HS20, (*d*) HS40 and (*e*) HS70 hybrid HA–chitosan nanoparticles.

results, that the interaction of chitosan with nHA crystallites does not seem to be a likely mechanism for the modulation of crystallization and assembly of nHA. There is some indirect indication that the chitosan molecules could have assumed a more linear conformation in the hybrid films, as observed in figure 6*e*. This indicated that chitosan chain stretching could have taken place during the drying stage facilitating the linear assembly of the nanoparticles. However, it is too early based on the present data to conclude or completely confirm chitosan chain stretching (and the mechanisms thereof) in the hybrid films, from spiralled or coiled conformation in the suspension.

The main highlight of this study, we think, was the finding that the cross-section of the films (figure 7) exhibited a unique structure that started with nanoparticles assembled at the bottom and a continuously changing structure that ended on top with a chitosan surface. It seems probable that the evolution of this graded film took place through mutual interaction of the organic and inorganic components over time and space. Even though the mechanisms of formation for this hybrid-graded film seem to be numerous and complex, we hypothesize for now that it proceeds with the phosphorylation of chitosan molecules during synthesis and its interaction with amorphous precursors to HA. Though the involvement of chitosan in regulating nHA growth and its subsequent assembly is implicated, verification of the degree of phosphorylation of chitosan and/or identification of other mechanisms (if any) involved in this process still need to be carried out. Also, the mechanism controlling the formation of structurally and compositionally graded hybrid films requires a detailed study in order to tailor the structure and composition of these hybrid nanostructured films and perhaps extend these phenomena to other hybrid-material systems. We are also carrying out TEM studies to temporally investigate the ordering process to discern the early stages involved in the evolution of these nanostructured films as a function of time and pH.

At present, given the unique compositional and structural grading observed in these films, we have envisioned several potential biomedical applications. These could include: (i) self-assembled nanostructures as coatings mimicking biological structures, for example in the case of cementum as applied to avulsed teeth reinsertion (at the interface between the jaw bone and dentine, where the inorganic surface can serve as an impermeable layer to calcification and the organic-rich surface for periodontal tissue and ligament reconstruction mediated by cellular locomotion) and (ii) specifically designed constructs for a combination of strategies for oral peptide delivery; for example, nanoparticulate-mediated drug uptake and tailored slower release from the nano-porous layers of the hybrid film. The $-NH_2$ groups of the polysaccharide construct can also be conjugated with thiols to improve mucoadhesion, and with protease inhibitors and permeation enhancers *ex* or *in situ* to improve the bioavailability of the peptide drug.

The potential application of such graded and structured material in oral peptide delivery was also demonstrated. Commercial insulin (100 IU ml^{-1}) was used for this purpose and the drug release rate was studied in simulated gastric fluid (SGF) and simulated intestinal fluid (SIF). The SGF and SIF were prepared following the USP-24 standards for SGF (NaCl 2.0 g l^{-1}, 2.6 g l^{-1} HCl (7.0 ml of 37 wt% HCl), pH 1.2) and SIF (KH_2PO_4 6.8 g in 250 ml DI water, 190 ml of 0.2 M NaOH and 560 ml DI water, pH 7.5). A UV/vis spectrophotometer (UV-Vis Spectrophotometer-6500, Shimadzu, Japan) was used to determine the concentration of insulin in the fluids. Insulin has a characteristic absorption at 271 nm and a calibration curve was obtained by measuring absorbance at this wavelength

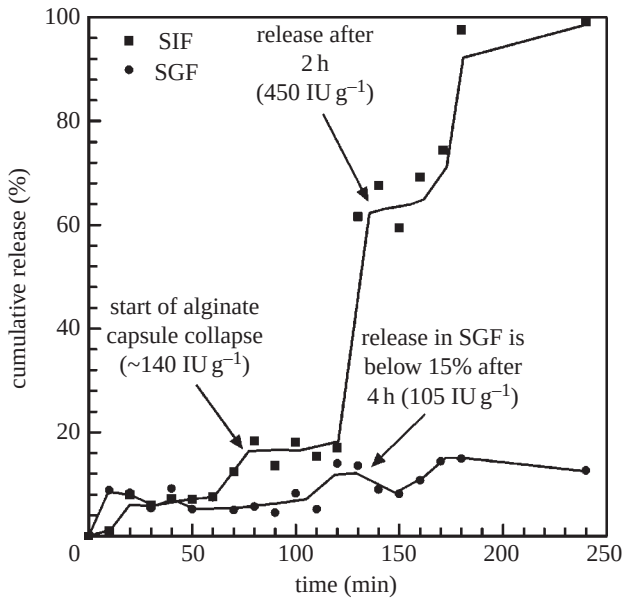

Figure 9. Release profile of insulin in SIF (squares) and SGF (circles) from loaded, encapsulated hybrid particles.

for a different insulin concentration solution. Insulin was loaded by soaking 25 mg of gently crushed HA–chitosan hybrid films in 1 ml of insulin at 4°C in a refrigerator overnight to maximize the degree of absorption and condensation. After soaking, the mixture was centrifuged at 10 000g and 0.1 ml of the supernatant was diluted with 1.9 ml of distilled water. The absorbance, and hence the concentration of insulin in the supernatant (S_1), was measured spectrophotometrically. The pellet, that is the insulin-loaded HA–chitosan hybrid particulate material, was then dried in the refrigerator overnight. To the dried particulates, 0.5 ml of sodium alginate (2 wt%) followed by 0.5 ml of $CaCl_2$ (1.5 wt%) was added and mildly stirred for 30 min to ensure enough time for a pH-sensitive encapsulation to form. Following this, the suspension was re-centrifuged and the concentration of insulin in the supernatant (S_2) was measured. The pellet was re-suspended in distilled water and gently agitated and centrifuged again. The concentration of insulin in the supernatant (S_3) was measured and the pellet was dried overnight at 4°C in the refrigerator. The insulin loaded, alginate-encapsulated HA–chitosan hybrid particulates were immersed in 20 ml of SGF and SIF, and were mildly agitated at 40g at 37°C. One millilitre of SGF and SIF was carefully removed from the container at regular time intervals and the concentration of insulin was measured. The same volume of fresh SGF and SIF was re-filled. The initial loading of insulin ($I_{t=0}$) in 25 mg of hybrid particles was calculated using equation (4.3).

$$I_{t=0} = S_0 - dV(S_1 + S_2 + S_3), \qquad (4.3)$$

where S_0 is the original insulin concentration (100 IU ml^{-1}); d is the dilution factor (20) and V is the volume of original insulin used (1 ml). The $I_{t=0}$ in 25 mg of hybrid particles was calculated to be about 17.5 IU (or 700 IU per gram of particulates).

Figure 9 shows the insulin release profile in both SGF and SIF up to 4 hours. The results showed that in SGF the release maintained a level of about 10–15% even up to 4 hours, whereas in SIF the release was about 65% of the calculated insulin loading after 2 hours and reached close to 100% release after 3 hours. The release profile in SIF suggested that the mechanism could be a combination of burst and slower release and the release in SGF might have been diminished owing to the alginate encapsulation. The results were promising, considering that experiments were preliminary trials, and not extensively designed or fully optimized. Even so, the trends did not follow simple release kinetics and seemed to be a function of several characteristics of the hybrid films. At first glance, there seems to be release taking place due to at least two contributing kinetic factors. For now, we think this release profile can be rationalized by considering the release of insulin bound with: (i) nanoparticles and (ii) the nano-hybrid architecture. At present, we are also studying the changes to the release profiles as a function of chitosan molecular weight, degree of deactylation and inclusion of thiolated (for mucoadhesion) and carbamide ammonium salts (for permeation enhancement) into the chitosan backbone.

5. CONCLUSIONS

The synthesis of nearly spherical nHA with a roughly 30 nm particle size has been carried out in the presence of the polysaccharide chitosan. TEM studies of the hybrid suspensions revealed that chitosan effectively modulated transformation kinetics of crystalline nHA growth and assembled the nano-crystals on its self-assembled spiral chains. This led to the observed and refined crystallite size and shape variations of nHA in the hybrid suspensions. The drying of the hybrid suspension formed nanostructured films incorporated with self-assembled nHA particles. The films also showed hierarchical ordering at several length-scales and were graded both structurally and compositionally from inorganic (HA) at the bottom to organic (chitosan) on the top, suggesting several interesting and novel biomedical applications as hybrid tissue engineering scaffolds and drug delivery devices.

REFERENCES

Andres, R. P., Bielefeld, J. D., Henderson, J. I., Janes, D. B., Kolagunta, V. R., Kubiak, C. P., Mahoney, W. J. & Osifchin, R. G. 1996 Self-assembly of a two-dimensional superlattice of molecularly linked metal clusters. *Science* **273**, 1690–1693. (doi:10.1126/science.273.5282.1690)

Boskey, A. L. & Posner, A. S. 1973 Conversion of amorphous calcium phosphate to microcrystalline hydroxyapatite. A pH-dependent, solution-mediated, solid–solid conversion. *J. Phys. Chem.* **77**, 2313–2317. (doi:10.1021/j100638a011)

Brugnerotto, J., Lizardi, J., Goycoolea, F. M., Arguelles-Monal, W., Desbrieres, J. & Rinaudo, M. 2001 An infrared investigation in relation with chitin and chitosan characterization. *Polymer* **42**, 3569–3580. (doi:10.1016/S0032-3861(00)00713-8)

Colfen, H. & Mann, S. 2003 Higher-order organization by mesoscale self-assembly and transformation of hybrid nanostructures. *Angew. Chem. Int. Ed.* **42**, 2350–2365. (doi:10.1002/anie.200200562)

Colfen, H. & Yu, S. H. 2005 Biomimetic mineralization/synthesis of mesoscale order in hybrid inorganic—organic materials via nanoparticle self-assembly. *MRS Bull.* **30**, 727–735.

Dabbs, D. M. & Aksay, I. A. 2000 Self-assembled ceramics produced by complex-fluid templation. *Annu. Rev. Phys. Chem.* **51**, 601–622. (doi:10.1146/annurev.physchem.51.1.601)

Elliot, J. C. 1994 *Structure and chemistry of the apatites and other calcium orthophosphates*. Amsterdam, The Netherlands: Elsevier.

Falini, G., Weiner, S. & Addadi, L. 2003 Chitin–silk fibroin interactions: Relevance to calcium carbonate formation in invertebrates. *Calcif. Tissue Int.* **72**, 548–554. (doi:10.1007/s00223-002-1055-0)

Galow, T. H., Boal, A. K. & Rotello, V. M. 2000 A "building block" approach to mixed-colloid systems through electrostatic self-organization. *Adv. Mater.* **12**, 576–579. (doi:10.1002/(SICI)1521-4095(200004)12:8<576::AID-ADMA576>3.0.CO;2-S)

Gower, L. B. & Odom, D. J. 2000 Deposition of calcium carbonate films by a polymer-induced liquid-precursor (PILP) process. *J. Cryst. Growth* **210**, 719–734. (doi:10.1016/S0022-0248(99)00749-6)

Gower, L. A. & Tirrell, D. A. 1998 Calcium carbonate films and helices grown in solutions of poly(aspartate). *J. Cryst. Growth* **191**, 153–160. (doi:10.1016/S0022-0248(98)00002-5)

Jiang, H., Liu, X.-Y., Zhang, G. & Yang, L. 2005 Kinetics and template nucleation of self-assembled hydroxyapatite nanocrystallites by chondroitin sulfate. *J. Biol. Chem.* **280**, 42 061–42 066. (doi:10.1074/jbc.M412280200)

Knowles, J. C., Gross, K. A., Berndt, C. C. & Bonfield, W. 1996 Structural changes of thermally sprayed hydroxyapatite investigated by Rietveld method. *Biomaterials* **17**, 639–645. (doi:10.1016/0142-9612(96)88715-1)

Kumar, R., Cheang, P. & Khor, K. A. 2004 Phase composition and heat of crystallisation of amorphous calcium phosphate in ultra-fine radio frequency suspension plasma sprayed hydroxyapatite powders. *Acta Mater.* **52**, 1171–1181. (doi:10.1016/j.actamat.2003.11.016)

Kumar, R., Prakash, K. H., Cheang, P. & Khor, K. A. 2005 Microstructure and mechanical properties of spark plasma sintered zirconia-hydroxyapatite nano-composite powders. *Acta Mater.* **53**, 2327–2335. (doi:10.1016/j.actamat.2005.01.039)

Lazic, S. 1995 Microcrystalline hydroxyapatite formation from alkaline solutions. *J. Cryst. Growth* **147**, 147–154. (doi:10.1016/0022-0248(94)00587-7)

Matevosyan, G. L., Yukha, Y. S. & Zavlin, P. M. 2003 Phosphorylation of chitosan. *Russ. J. Gen. Chem.* **73**, 1725–1728. (doi:10.1023/B:RUGC.0000018648.18120.18)

McCusker, L. B., Von Dreele, R. B., Cox, D. E., Louer, D. & Scardi, P. 1999 Rietveld refinement guidelines. *J. Appl. Cryst.* **32**, 36–50. (doi:10.1107/S0021889898009856)

Meyer, J. L. & Weatherall, C. C. 1982 Amorphous to crystalline calcium phosphate phase transformation at elevated pH. *J. Coll. Interface Sci.* **89**, 257–267. (doi:10.1016/0021-9797(82)90139-4)

Murray, C. B., Kagan, C. R. & Bawendi, M. G. 1995 Self-organization of CdSe nanocrystallites into 3-dimensional quantum-dot superlattices. *Science* **270**, 1335–1338. (doi:10.1126/science.270.5240.1335)

Nancollas, G. H. & Tomazic, B. 1974 Growth of calcium phosphate on hydroxyapatite crystals. Effect of supersaturation and ionic medium. *J. Phys. Chem.* **78**, 2218–2225. (doi:10.1021/j100615a007)

Nishi, N., Ebina, A., Nishimura, S. I., Tsutsumi, A., Hasegawa, O. & Tokura, S. 1986 Highly phosphorylated derivatives of chitin, partially deacetylated chitin and chitosan as new functional polymers: preparation and characterization. *Int. J. Bio. Macromol.* **8**, 311–317. (doi:10.1016/0141-8130(86)90046-2)

Olszta, M. J., Douglas, E. P. & Gower, L. B. 2003*a* Intrafibrillar mineralization of collagen using a liquid-phase mineral precursor. In *Materials research society symposium: Materials inspired by biology* (eds J. Thomas, K. Kiick & L. Gower), pp. 127–134. San Francisco, CA: MRS.

Olszta, M. J., Douglas, E. P. & Gower, L. B. 2003*b* Scanning electron microscopic analysis of the mineralization of type I collagen via a polymer-induced liquid-precursor (PILP) process. *Calcif. Tissue Int.* **72**, 583–591. (doi:10.1007/s00223-002-1032-7)

Pedroni, V. I., Schulz, P. C., Gschaider, M. E. & Andreucetti, N. 2003 Chitosan structure in aqueous solution. *Coll. Polym. Sci.* **282**, 100–102. (doi:10.1007/s00396-003-0965-3)

Penel, G., Leroy, G., Rey, C., Sombret, B., Huvenne, J. P. & Bres, E. 1997 Infrared and Raman microspectrometry study of fluor-fluor-hydroxy and hydroxy-apatite powders. *J. Mater. Sci. Mater. Med.* **8**, 271–276. (doi:10.1023/A:1018504126866)

Popa, N. C. 1998 The (hkl) dependence of diffraction-line broadening caused by strain and size for all Laue groups in Rietveld refinement. *J. Appl. Cryst.* **31**, 176–180. (doi:10.1107/S0021889897009795)

Prakash, K. H., Kumar, R., Ooi, C. P., Cheang, P. & Khor, K. A. 2006 Conductometric study of precursor compound formation during wet-chemical synthesis of nanocrystalline hydroxyapatite. *J. Phys. Chem. B* **110**, 24 457–24 462. (doi:10.1021/jp065200x)

Rehman, I. & Bonfield, W. 1997 Characterization of hydroxyapatite and carbonated apatite by photo acoustic FTIR spectroscopy. *J. Mater. Sci. Mater. Med.* **8**, 1–4. (doi:10.1023/A:1018570213546)

Rhee, S. H. & Tanaka, J. 2000 Effect of chondroitin sulfate on the crystal growth of hydroxyapatite. *J. Am. Ceram. Soc.* **83**, 2100–2102.

Rhee, S. H. & Tanaka, J. 2001 Synthesis of a hydroxyapatite/collagen/chondroitin sulfate nanocomposite by a novel precipitation method. *J. Am. Ceram. Soc.* **84**, 459–461.

Rusu, V. M., Ng, C.-H., Wilke, M., Tiersch, B., Fratzl, P. & Peter, M. G. 2005 Size-controlled hydroxyapatite nanoparticles as self-organized organic–inorganic composite materials. *Biomaterials* **26**, 5414–5426. (doi:10.1016/j.biomaterials.2005.01.051)

Sigel, H. & Martin, R. B. 1982 Coordinating properties of the amide bond. Stability and structure of metal ion complexes of peptides and related ligands. *Chem. Rev.* **82**, 385–426. (doi:10.1021/cr00050a003)

van Kemenade, M. J. J. M. & de Bruyn, P. L. 1987 A kinetic study of precipitation from supersaturated calcium phosphate solutions. *J. Coll. Interface Sci.* **118**, 564–585. (doi:10.1016/0021-9797(87)90490-5)

Varma, H. K., Yokogawa, Y., Espinosa, F. F., Kawamoto, Y., Nishizawa, K., Nagata, F. & Kameyama, T. 1999 Porous calcium phosphate coating over phosphorylated chitosan film by a biomimetic method. *Biomaterials* **20**, 879–884. (doi:10.1016/S0142-9612(98)00243-9)

Varma, A. J., Deshpande, S. V. & Kennedy, J. F. 2004 Metal complexation by chitosan and its derivatives: a review. *Carbohydrate Polym.* **55**, 77–93. (doi:10.1016/j.carbpol.2003.08.005)

Wan, Y., Creber, K. A. M., Peppley, B. & Bui, V. T. 2003 Synthesis, characterization and ionic conductive properties of phosphorylated chitosan membranes. *Macromol. Chem. Phys.* **204**, 850–858. (doi:10.1002/macp.200390056)

Wang, Z. L. 1998 Structural analysis of self-assembling nanocrystal superlattices. *Adv. Mater.* **10**, 13–30. (doi:10.1002/(SICI)1521-4095(199801)10:1<13::AID-ADMA13>3.0.CO;2-W)

Yamaguchi, I., Tokuchi, K., Fukuzaki, H., Koyama, Y., Takakuda, K., Monma, H. & Tanaka, J. 2000 Preparation and mechanical properties of chitosan/hydroxyapatite nanocomposites. *Bioceramics* **192**, 673–676.

Yamaguchi, I., Tokuchi, K., Fukuzaki, H., Koyama, Y., Takakuda, K., Monma, H. & Tanaka, T. 2001 Preparation and microstructure analysis of chitosan/hydroxyapatite nanocomposites. *J. Biomed. Mater. Res.* **55**, 20–27. (doi:10.1002/1097-4636(200104)55:1<20::AID-JBM30>3.0.CO;2-F)

Yi, H. M., Wu, L. Q., Bentley, W. E., Ghodssi, R., Rubloff, G. W., Culver, J. N. & Payne, G. F. 2005 Biofabrication with chitosan. *Biomacromolecules* **6**, 2881–2894. (doi:10.1021/bm050410l)

Yokogawa, Y., Nishizawa, K., Nagata, F. & Kameyama, T. 2001 Bioactive properties of chitin/chitosan–calcium phosphate composite materials. *J. Sol-Gel Sci. Technol.* **21**, 105–113. (doi:10.1023/A:1011222003264)